PAPER

Ternary PdNiO nanocrystals-ornamented porous CeO$_2$/onion-like carbon for electrooxidation of carbon monoxide: unveiling the effect of supports and electrolytes†

Adewale K. Ipadeola, [iD] [ab] Aderemi B. Haruna,[c] Aboubakr M. Abdullah,*[a] Rashid S. Al-Hajri,[d] Roman Viter,[e] Kenneth I. Ozoemena [iD] *[c] and Kamel Eid [iD] *[b]

Porous ternary Pd-based catalysts are highly promising for various electrocatalytic applications, due to their low Pd mass, high surface area, accessible active sites, and tunable electronic structure; however, their activity for CO oxidation (CO$_{oxid}$) in different electrolytes is yet to be reported. Herein, ternary PdNiO nanocrystals supported on porous CeO$_2$/onion-like carbon nanostructures (PdNiO–CeO$_2$/OLC) were prepared by the sol–gel and impregnation approaches for electrochemical CO$_{oxid}$ in different electrolytes at room temperature. Notably, porous CeO$_2$/OLC acts as a support and nanoreactor for supporting the growth of PdNiO without the need for reducing agents or surfactants. The as-obtained PdNiO–CeO$_2$/OLC had a porous sponge-like structure composed of ultra-small PdNiO nanocrystals (8 ± 1 nm) distributed on porous flower-like CeO$_2$ and OLC, which possessed unique merits of multifunctional structure, clean surface, low mass of Pd (10 wt%), porosity (0.30 cm^3 g^{-1}), and high surface area (155.66 m^2 g^{-1}). The CO$_{oxid}$ activity of PdNiO–CeO$_2$/OLC was higher than those of PdNiO/OLC, PdNiO–CeO$_2$, and commercial Pd/C catalyst, owing to the electronic interaction of PdNiO with CeO$_2$/OLC support, which eases CO adsorption/activation alongside activation/dissociation of H$_2$O to generate active oxygenated species (*i.e.*, OH) needed for accelerating CO$_{oxid}$ kinetics. The CO$_{oxid}$ activity of PdNiO–CeO$_2$/OLC in acidic electrolyte (HClO$_4$) was better than those in alkaline (KOH) and neutral (NaHCO$_3$) electrolytes. This study may open new doorways for understanding the effect of electrolytes and supports on the CO$_{oxid}$ activity of porous ternary Pd-based catalysts.

Introduction

Electrochemical energy conversion utilizing different fuels, like water[1–3] and small-molecule organic compounds,[1,4,5] has emerged as one of the most promising renewable systems to replace the use of fossil fuels.[1,2] However, carbon monoxide (CO) is a hindrance to the optimal operation of energy conversion systems because of its strong adsorption properties that devalue electrodes by blocking their active sites.[6–9] Hence, studies have proved CO oxidation (CO$_{oxid}$) to be a prototypical reaction for heterogeneous catalytic processes with industrial and environmental applications,[10–16] as it is converted to reusable fuels and suitable organic chemicals with efficient electrodes rather than deactivating them.[17–20] Electrochemical CO$_{oxid}$ is predominantly preferred to thermal CO$_{oxid}$, owing to its low energy/power consumption, high stability, and selectivity.[21–24] Hence, electrochemical CO$_{oxid}$ necessitates electrocatalysts that are tolerant to CO poisoning and convert it to useful products. Amongst the most sought-after electrocatalysts, palladium (Pd) is highly active and durable for CO$_{oxid}$ electrocatalysis, due to the quick CO activation/adsorption and O$_2$ dissociation energies at low overpotential.[25–29] However, practical application is hindered because of the high cost, scarcity, and carbonaceous species poisoning of Pd.

Efficient and durable Pd-based electrocatalysts are strategically prepared by adjusting their sizes, compositions,

[a] *Center for advanced materials, Qatar University, Doha 2713, Qatar. E-mail: bakr@qu.edu.qa*

[b] *Gas Processing Center (GPC), College of Engineering, Qatar University, Doha 2713, Qatar. E-mail: kamel.eid@qu.edu.qa*

[c] *Molecular Sciences Institute, School of Chemistry, University of the Witwatersrand, Private Bag 3, PO Wits, Johannesburg 2050, South Africa. E-mail: Kenneth.ozoemena@wits.ac.za*

[d] *Petroleum and Chemical Engineering Department, Sultan Qaboos University, Muscat, Oman*

[e] *Institute of Atomic Physics and Spectroscopy, University of Latvia, 19 Raina Blvd., LV-1586 Riga, Latvia*

† Electronic supplementary information (ESI) available. See DOI: https://doi.org/10.1039/d3cy00253e

This journal is © The Royal Society of Chemistry 2023

Catal. Sci. Technol., 2023, 13, 3035–3046 | 3035

and morphologies supported on unique carbon platforms (*i.e.*, onion-like carbon (OLC), carbon black (CB), carbon nanotubes, graphene *etc.*) to boost their electrical conductivity, charge mobility, and stability against aggregation.[30–32] The impressive physicochemical merits of the OLC, including zero-dimensional concentric shell-like structures, nanosized diameter (<10 nm), high electrical conductivity and stability, low toxicity, and large surface area, are advantageous for improving Pd nanocatalysts' performance.[33–35] Also, alloying Pd with earth-abundant and inexpensive transition metal oxides (M = CeO_2, TiO_2, Co_2O_3, Fe_2O_3, MnO_2 *etc.*) modifies its d-band centre close to the Fermi level that enable quick CO adsorption/activation on the active sites, besides the spillover effect that generates reactive oxygenated species (*i.e.*, OH radicals) from H_2O splitting,[36–41] which are advantageously utilized for efficient electrocatalysis.[25,42–46] For example, the addition of CeO_2 to Pd/OLC (Pd–CeO_2/OLC) significantly increased its hydrogen oxidation reaction (HOR) electrocatalytic activity by 13.2 and 15.0 times compared with Pd/OLC and Pd/CB, respectively, due the induced defects and modified electronic structure of Pd/OLC interfaced by CeO_2.[47] Hence, CeO_2/OLC composite support enables great interfacial interaction with Pd for great electrocatalysis. The CO_{oxid} mechanism includes the adsorption of CO on Pd active sites and its removal by oxygen-containing species (*i.e.*, OH). The spillover effect of co-metal oxides in the Pd-based nanocrystals promoted the generation of OH species for easy desorption of adsorbed CO, resulting in enhanced CO_{oxid} electrocatalysis.[48–51] NiO/CeO_2 showed high performance for electrooxidation of organic solvents (methanol, ethanol, phenol, *etc.*).[52] The NiO/CeO_2 composites due to higher concentration of surface sites promoted enhanced adsorption of CO and interaction with oxygen species.[53] It was reported that Ni/Ce interface showed high electron coupling and supported adsorption of OH^-, suitable for fast electrooxidation applications.[54,55]

Binary Pd-based nanocrystals are mostly fabricated for electrochemical CO_{oxid}. For example, Pd/Ni nanocrystals embedded on metal–organic framework-derived porous carbon nanosheets (Pd/Ni-MOF/PC) gave higher CO_{oxid} activity compared to Pd/C in acid, alkaline, and neutral conditions by factors of 5.0, 2.9, and 2.3, respectively, because of the large pores and abundant active sites of Pd/Ni–N_x in Pd/Ni-MOF/PC that enabled fast diffusion of reactant/intermediate species, CO activation/desorption and O_2 dissociation at low overpotential.[56] Similarly, the coordination of Pd and Co–N_x in Pd/ZIF-67/C significantly improved its CO_{oxid} electrocatalytic activity by 4.2- and 4.4-fold compared with Pd/C in $HClO_4$ electrolyte, owing to the synergy between the catalytic merits of Pd (*i.e.*, facile CO activation/adsorption and O_2 dissociation at low potential) and physicochemical features of ZIF-67/C (*i.e.*, porosity, rich electron density, defects, and electrical conductivity).[22] Also, Rh nanoparticles were reported to effectively promote the CO_{oxid} catalysis of zeolite.[57] As far as we are aware, there is no report on the use of ternary Pd-based nanocrystals for

CO_{oxid} electrocatalysis, let alone using the OLC platform. Ternary Pd-based nanocrystals are expected to further improve the d-band centre, whereas OLC increases the electron/charge mobility that is maximally utilized for excellent CO_{oxid}. Although there have been great achievements in the synthesis of porous ternary Pd-based catalysts, their utilization in electrochemical CO_{oxid} is not yet reported. Also, the effect of electrolyte and support on the CO_{oxid} activity of porous ternary Pd-based electrocatalysts remains ambiguous.

This article reports the controlled fabrication of ternary PdNiO nanocrystals supported on porous CeO_2/OLC nanostructures (PdNiO–CeO_2/OLC). The synthetic approach entails the annealing of diamond to form OLC, then undergone sol–gel method with cerium salt to form flower-like CeO_2/OLC nanostructure and then impregnation with Pd/Ni precursors to form porous sponge-like PdNiO–CeO_2/OLC. The fabrication mechanism is attributed to the ability of CeO_2/OLC to act as a reactor for promoting the reduction and growth of PdNiO in the absence of reducing agents or surfactants or organic solvents. The surface and bulk characterization techniques evidenced the good contact of porous PdNiO nanocrystals with 3D flower-like CeO_2 and OLC nanostructures, which combine inimitable properties of the multifunctional structure, clean surface, low mass of Pd (10 wt%), porosity (0.30 cm^3 g^{-1}), and large surface area (155.66 m^2 g^{-1}). To investigate the effect of electrolytes and supports on the catalytic performance of PdNiO–CeO_2/OLC, its electrochemical CO_{oxid} performance was tested and compared with that of PdNiO/OLC, PdNiO–CeO_2, and commercial Pd/C in KOH, $NaHCO_3$, and $HClO_4$ electrolytes.

Experimental

Chemicals and materials

Cerium(II) nitrate hexahydrate ($Ce(NO_3)_3 \cdot 6H_2O$, ≥99%), nickel(II) chloride hexahydrate ($NiCl_2 \cdot 6H_2O$, ≥99%), potassium palladium(II) chloride (K_2PdCl_4, ≥98%), potassium hydroxide pellets (KOH, ≥85%), anhydrous sodium bicarbonate ($NaHCO_3$, 99.999%), perchloric acid ($HClO_4$, 70%), and commercial Pd/C catalyst (Pd, 10 wt%) were purchased from Sigma-Aldrich Chemie GmbH (Munich, Germany).

Preparation of PdNiO–CeO_2/OLC, PdNiO/OLC, and PdNiO–CeO_2 electrocatalysts

OLC was prepared by the direct annealing of high-purity nanodiamond powder in a muffle furnace at 1300 °C for 3 h in Ar as reported before.[58] CeO_2/OLC was prepared by mixing an aqueous solution of $Ce(NO_3)_3$ (1.50 g) and OLC (1.13 g) at pH 12 under magnetic stirring and heating at 80 °C for 1.5 h. The obtained black precipitate was centrifuged at 7000 rpm, washed with deionized water and dried at 80 °C for 1 h and then annealed at 250 °C for 2 h under air.

Hierarchical porous PdNiO–CeO_2/OLC nanostructure was synthesized by mixing aqueous solutions, containing K_2PdCl_4 (0.12 g), $NiCl_2$ (0.15 g), NaOH (pH 12), and CeO_2/OLC (0.30 g), under sonication at 25 °C for 30 min and then kept under

3036 | *Catal. Sci. Technol.*, 2023, **13**, 3035–3046

This journal is © The Royal Society of Chemistry 2023

reflux at 80 °C for 1 h. Finally, PdNiO–CeO$_2$/OLC was purified *via* consecutive centrifugation at 7000 rpm for 20 min and washed severally with deionized water.

PdNiO/OLC and PdNiO/CeO$_2$ were also prepared by the same method as that for PdNiO–CeO$_2$/OLC, but in the absence of CeO$_2$ or OLC supports, respectively.

Materials characterization

The as-formed nanocatalysts were characterized by a scanning electron microscope (SEM, S-4800, Hitachi, Tokyo, Japan) equipped with an energy dispersive X-ray analyzer (EDX) and a transmission electron microscope (TEM, TecnaiG220, FEI, Hillsboro, USA). X-ray photoelectron spectroscopy (XPS) was conducted with an Ultra DLD XPS (Kratos, Manchester, UK). X-ray diffraction (XRD) patterns were collected with an X'Pert-Pro MPD (PANalytical Co., Almelo, Netherlands). The N$_2$ adsorption–desorption isotherm was conducted with a Micromeritics TriStar II 3000. Thermal gravimetric analysis was conducted with a PerkinElmer thermogravimetric analyzer (TGA 6000). Inductively coupled plasma optical emission spectrometry (ICP-OES) was conducted with an Agilent 5800 (USA).

Electrochemical CO oxidation measurements

The electrochemical CO$_{oxid}$ was conducted with a Gamry potentiostat (Reference 3000, Gamry Co., Warminster, PA,
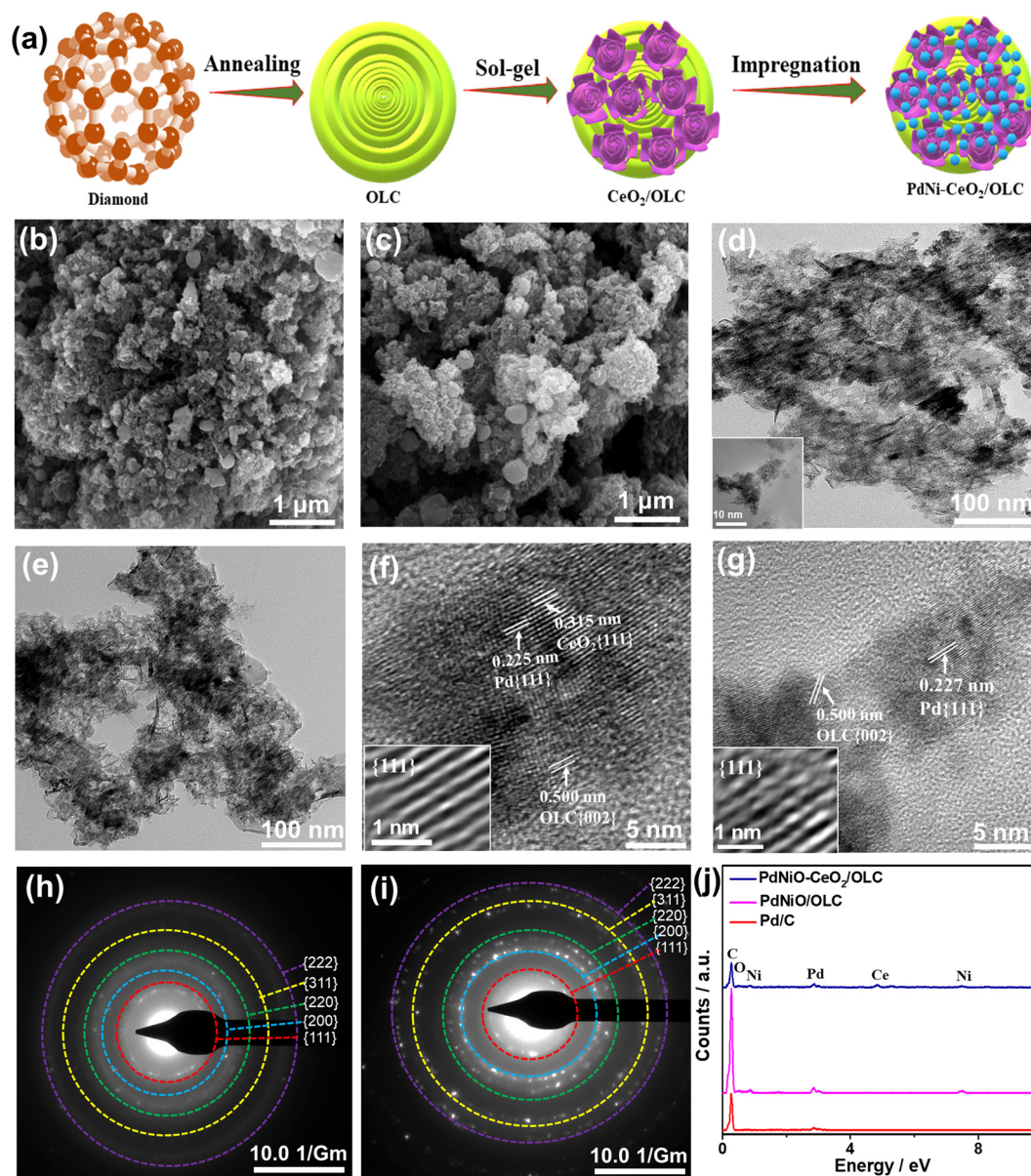

Fig. 1 (a) Schematic preparation method. (b and c) SEM images, (d and e) TEM micrographs, (f and g) HRTEM images with Fourier-transform HRTEM, and (h and i) SAED patterns of PdNiO–CeO$_2$/OLC and PdNiO/OLC, respectively, and (j) EDX analysis.

This journal is © The Royal Society of Chemistry 2023

Catal. Sci. Technol., 2023, **13**, 3035–3046 | **3037**

USA) using a three-electrode cell, consisting of Pt wire as a counter electrode, Ag/AgCl (KCl, 3 M) as reference electrode, and glassy carbon electrode (GCE) as a working electrode. The catalyst inks were prepared by dispersing each electrocatalyst (2 mg) in ethanol/H_2O/Nafion (0.05 wt) (3/1/1 v/v/v ratio) and drop-casting onto the polished GCE and then left to dry in an oven under vacuum at 50 °C for 2 h before measurements. The mass loading of the Pd on the GCE was about 0.01 mg_{Pd} cm^{-2} as determined by ICP-OES. Cyclic voltammetry (CV), linear sweep voltammetry (LSV), electrochemical impedance spectroscopy (EIS), and chronoamperometry (CA) tests were carried out in aqueous solutions of $HClO_4$, KOH, and $NaHCO_3$ electrolytes at room temperature. The electrochemical active surface area (ECSA) of the nanocatalysts was determined by eqn (1):

$$ECSA = Q/(S \times m) \qquad (1)$$

where Q is the integrated charges in hydrogen underpotential deposition–desorption area obtained after the double layer correction, m is the Pd loading amount on the electrode, and 0.424 mC cm^{-2} is the charge required for the monolayer adsorption of H_2 on the Pd surface.

Results and discussion

Fig. 1a shows the fabrication process of PdNiO–CeO_2/OLC involving the initial preparation of porous flower-like CeO_2/OLC nanostructure *via* the sol–gel approach in the presence of the as-prepared OLC.[58] Notably, adjusting the pH to 12 is the key to inducing the formation of a black precipitate; meanwhile, this method is green and allows the production of uniform flower-like CeO_2 well dispersed over OLC. The as-formed CeO_2/OLC was then impregnated with aqueous solutions of K_2PdCl_4 and $NiCl_2$ at pH 12 under sonication and then refluxed at 80 °C for 1 h to form porous sponge-like PdNiO–CeO_2/OLC nanostructure. CeO_2/OLC somehow acts as a reactor for prompt reduction and growth of PdNiO nanocrystals without the need for reducing agents or surfactants, which is plausibly attributed to the negative reduction potential of CeO_2/OLC relative to Pd and Ni ions. This is evidenced by the SEM images which reflect the formation of PdNiO–CeO_2/OLC (Fig. 1b) and PdNiO/OLC (Fig. 1c) in 3D porous sponge-like nanostructure, whereas Pd/C possesses 3D spherical nanostructures (Fig. S1a†). The TEM images demonstrate that PdNiO–CeO_2/OLC is composed of small PdNiO nanocrystals (2.54 nm) well anchored on flower-like CeO_2 (20 nm) and OLC (30 nm) as indicated by the arrows in Fig. 1d, only porous sheets of PdNiO (4.34 nm) on OLC (30 nm) in PdNiO/OLC (Fig. 1e), and nanospheres of Pd (7.25 nm) in Pd/C (Fig. S1b and S2†). The good contact of PdNiO over CeO_2/OLC is highly beneficial for its stabilization as well as electronic interaction during electrocatalytic CO oxidations, while porosity is important for maximizing atomic utilization and providing accessible active sites.

The HRTEM micrographs of PdNiO–CeO_2/OLC, PdNiO/OLC, and Pd/C show the lattice fringes with multiple crystalline defects (*i.e.*, interfacial dislocation, intragranular dislocation, and stacking fault) as indicated by the lines in Fig. 1f and g and S1c.† Also, the lattice fringes are distributed in various directions, which implies the non-epitaxial growth of PdNiO, as usually observed in the formation of binary and ternary Pd-based catalysts. The defects may act as active catalytic sites during CO_{oxid}. The *d*-spacing of the resolved lattice fringes of PdNiO–CeO_2/OLC is estimated to be 0.225 nm that is assigned to {111} facet of face-centred cubic (fcc) Pd, {111} index of CeO_2 (0.315 nm), and {002} facet of OLC (0.500 nm) (Fig. 1f). Likewise, the resolved lattice fringes of PdNiO/OLC have a higher *d*-spacing of 0.227 nm for {111} facet of fcc Pd and 0.500 nm for {002} index of OLC, which are distributed in a different direction, but with fewer defects than PdNiO–CeO_2/OLC (Fig. 1g). Pd/C has the highest *d*-spacing of 0.232 nm (Fig. S1c†). The selected area electron diffraction (SAED) patterns of PdNiO–CeO_2/OLC and PdNiO/OLC reveal typical rings of {111}, {200}, {220}, {311}, and {222} facet of fcc Pd (Fig. 1h and i and S1d†). The EDX analysis reveals the existence of Pd/Ni/Ce/O/C in PdNiO–CeO_2/OLC and Pd/Ni/C in PdNiO/OLC with atomic contents of 0.74/1.30/0.79/9.26/87.91% and 0.73/0.49/98.78%, respectively (Fig. 1j). The ICP-OES analysis reveals that the atomic contents are 9.79/11.47/29.37% for Pd/Ni/Ce in PdNiO–CeO_2/OLC and 10.27/11.79% for Pd/Ni in PdNiO/OLC.

The XRD analyses of PdNiO–CeO_2/OLC, PdNiO/OLC, PdNiO–CeO_2, and Pd/C demonstrate the diffraction patterns assigned to {111}, {200}, {220}, {311}, and {222} facets of fcc Pd, besides {002} facet of graphitic carbon and two additional peaks assigned to {111} and {220} facets of NiO in PdNiO–CeO_2/OLC and PdNiO/OLC (Fig. 2a). Notably, the diffraction peaks of PdNiO–CeO_2/OLC are slightly shifted positively towards a higher 2θ angle, relative to those of PdNiO/OLC and Pd/C. This is due to the interaction of PdNiO with CeO_2/OLC, which leads to the lattice contraction of Pd, which occurs *via* the integration of NiO and electronic interaction with CeO_2/OLC. This is shown in the lower Pd crystallite sizes on the integration of NiO and NiO–CeO_2, besides the lower crystallite sizes of PdNiO–CeO_2/OLC (7.19 nm) than those of PdNiO/OLC (8.68 nm) and Pd/C (9.03 nm), except PdNiO–CeO_2 (7.02 nm), as determined from the Scherrer equation.

The XPS full-survey scans display the valence states of Pd3d/Ni2p/Ce3d/O1s/C1s in PdNiO–CeO_2/OLC, Pd3d/Ni2p/C1s in PdNiO/OLC, and Pd3d/C1s in Pd/C catalyst. The surface atomic contents of PdNiO–CeO_2/OLC (Pd3d/Ni2p/Ce3d/O1s/C1s) are 10.61/9.85/11.21/15.87/52.46%, of PdNiO/OLC (Pd3d/Ni2p/C1s) are 9.90/6.03/84.07%, and of Pd/C (Pd3d/C1s) are 9.99/90.1% (Fig. 2b). The fitting of Pd3d spectra of PdNiO–CeO_2/OLC, PdNiO/OLC, and Pd/C display Pd^0($3d_{5/2}$ and $3d_{3/2}$) metallic phase as the major phase, besides the minor oxide phase of Pd^{2+}($3d_{5/2}$ and $3d_{3/2}$)[29] (Fig. 2c–e). The ratio of Pd^0/Pd^{2+} is around 80% in both PdNiO–CeO_2/OLC and PdNiO/OLC. However, the binding

3038 | *Catal. Sci. Technol.*, 2023, **13**, 3035–3046

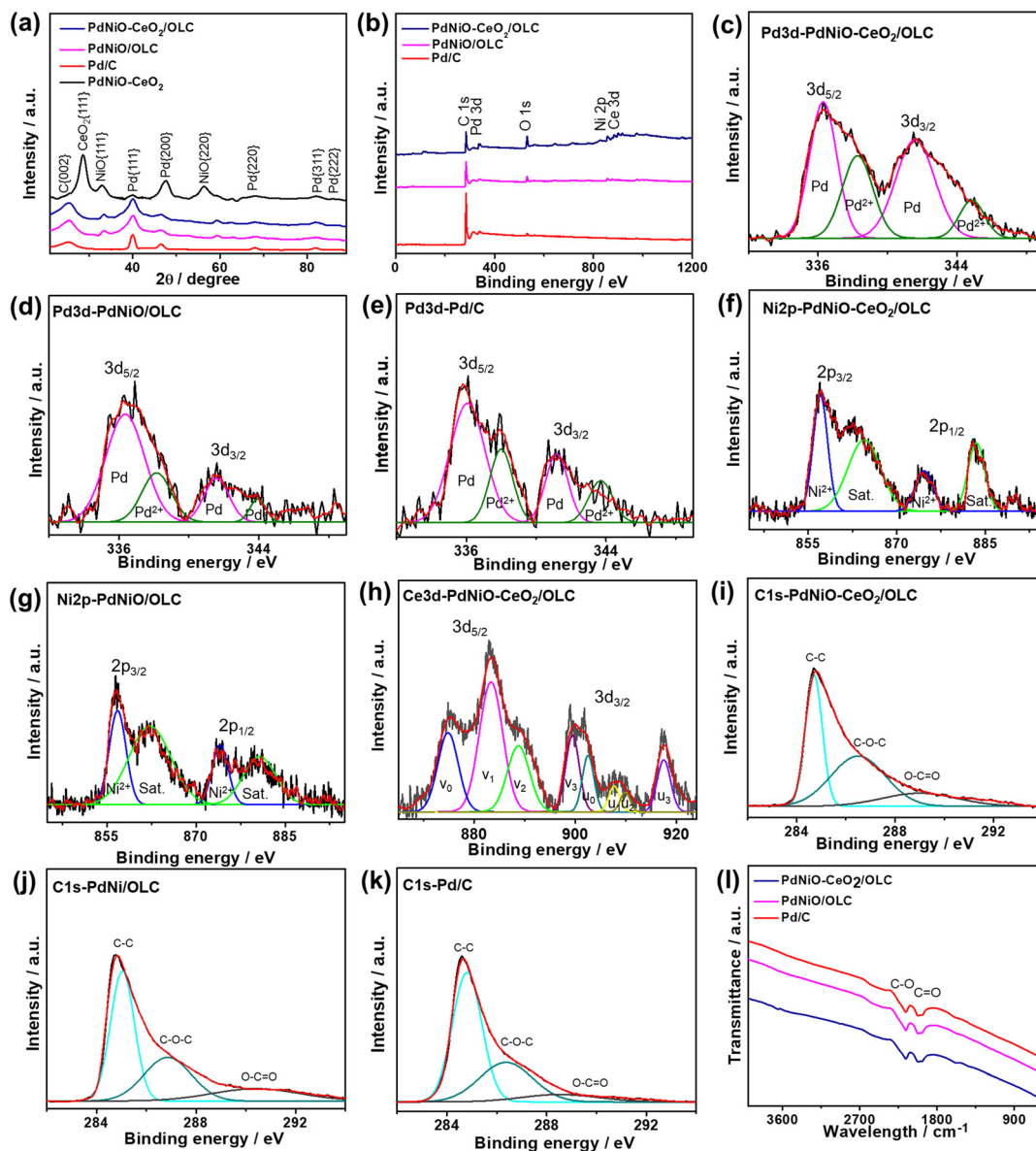This journal is © The Royal Society of Chemistry 2023

Fig. 2 (a) XRD patterns, (b) XPS wide-survey scans, high-resolution XPS spectra of (c–e) Pd3d, (f and g) Ni2p, (h) Ce3d, (i–k) C1s, and (l) FTIR spectra of PdNiO–CeO$_2$/OLC, PdNiO/OLC, PdNiO–CeO$_2$, and Pd/C nanocrystals.

energies of Pd3d in PdNiO–CeO$_2$/OLC are slightly shifted negatively relative to those in PdNiO/OLC and Pd/C, which serve as evidence for the increased d-band center of Pd in PdNiO–CeO$_2$/OLC. This is plausibly owing to the interfacial interaction of PdNiO and its electronic interaction with CeO$_2$ and OLC supports, *i.e.*, increased screening of the Pd 3d nucleus by the Ce^{4+} 3d conduction band. Modulating the d-band center of Pd is one of the most efficient strategies to induce the adsorption and activation of reactants along with tolerating the adsorption of poisoning species during electrocatalytic oxidation reactions. The deconvolution of Ni2p spectra of PdNiO–CeO$_2$/OLC and PdNiO/OLC reveals the major metal oxide phase of Ni^{2+}(3d$_{5/2}$ and 3d$_{3/2}$) and their satellites (Fig. 2f and g); likewise, Ce3d spectra show the mixed

oxide phases of Ce^{3+}(3d$_{5/2}$ and 3d$_{3/2}$) representing v_1 and u_1, while those of Ce^{4+}(3d$_{5/2}$ and 3d$_{3/2}$) are denoted as v_0, v_2, v_3, u_0, u_2 and u_3 in PdNiO–CeO$_2$/OLC (Fig. 2h).

The C1s spectra are deconvoluted into C=C as the main phase, besides C–O and C=O phases in PdNiO–CeO$_2$/OLC, PdNiO/OLC, and Pd/C (Fig. 2i–k).

The FTIR analysis of PdNiO–CeO$_2$/OLC and PdNiO/OLC displays stretching vibration bands at 1868–2087 cm^{-1} of C=O vibration and at 2087–2334 cm^{-1} for C–O vibration (Fig. 2l). The bands of surface functional groups in PdNiO–CeO$_2$/OLC are slightly broader than that in PdNiO/OLC, implying the better electronic interaction between PdNiO and CeO$_2$/OLC.

The N$_2$ adsorption–desorption isotherm and pore radius distribution of PdNiO–CeO$_2$/OLC and PdNiO/OLC reveal the

This journal is © The Royal Society of Chemistry 2023

Catal. Sci. Technol., 2023, **13**, 3035–3046 | **3039**

features close to those of a type IV curve with an H4 hysteresis loop, but with a larger area at $0.35 < P/P_0 < 0.9$ and two-step capillary condensation at $P/P_0 < 0.1$ and $P/P_0 > 0.9$ in PdNiO–CeO$_2$/OLC, implying its multiple pores and higher surface area (Fig. S3†). Thereby, the surface area of PdNiO–CeO$_2$/OLC (155.66 m^2 g^{-1}) is greater than that of PdNiO/OLC (119.70 m^2 g^{-1}) as calculated using the Brunauer–Emmett–Teller (BET) model from integrating the isotherm curves. Meanwhile, the pore volume of PdNiO–CeO$_2$/OLC (0.30 cm^3 g^{-1}) is slightly higher than that of PdNiO/OLC (0.28 cm^3 g^{-1}), besides multiple pore size distribution ranging from 10 nm to 90 nm. The high surface area and multimodal porosity of PdNiO–CeO$_2$/OLC are beneficial for providing accessible sites, enhancing reactant diffusion, and maximizing the utilization of active sites during electrocatalytic CO$_{oxid}$.

The electrocatalytic CO$_{oxid}$ activities of PdNiO–CeO$_2$/OLC, PdNiO/OLC, and PdNiO–CeO$_2$ are benchmarked relative to Pd/C at wide pH ranges. The CV profiles of PdNiO–CeO$_2$/OLC, PdNiO/OLC, PdNiO–CeO$_2$, and Pd/C tested in N$_2$-saturated HClO$_4$ (0.1 M) present the standard voltammogram signatures for Pd-based catalysts, including double-layer hydrogen adsorption/desorption (H$_{ads/des}$) and redox peaks of Pd (Fig. 3a). Notably, the onset potential (E_{Onset}) of OH$^-$ adsorption on PdNiO–CeO$_2$/OLC (0.78 V) is lower than those on PdNiO/OLC (0.80 V), PdNiO–CeO$_2$ (0.80 V), and Pd/C (0.83 V), indicating the ease of H$_2$O activation and subsequent OH$^-$ adsorption on PdNiO in PdNiO–CeO$_2$/OLC, resulting from the electronic interaction with CeO$_2$/OLC.

Also, the Pd–O reduction peak of PdNiO–CeO$_2$/OLC is slightly shifted negatively to a lower potential than those of PdNiO/OLC, PdNiO–CeO$_2$, and Pd/C catalysts, indicating the
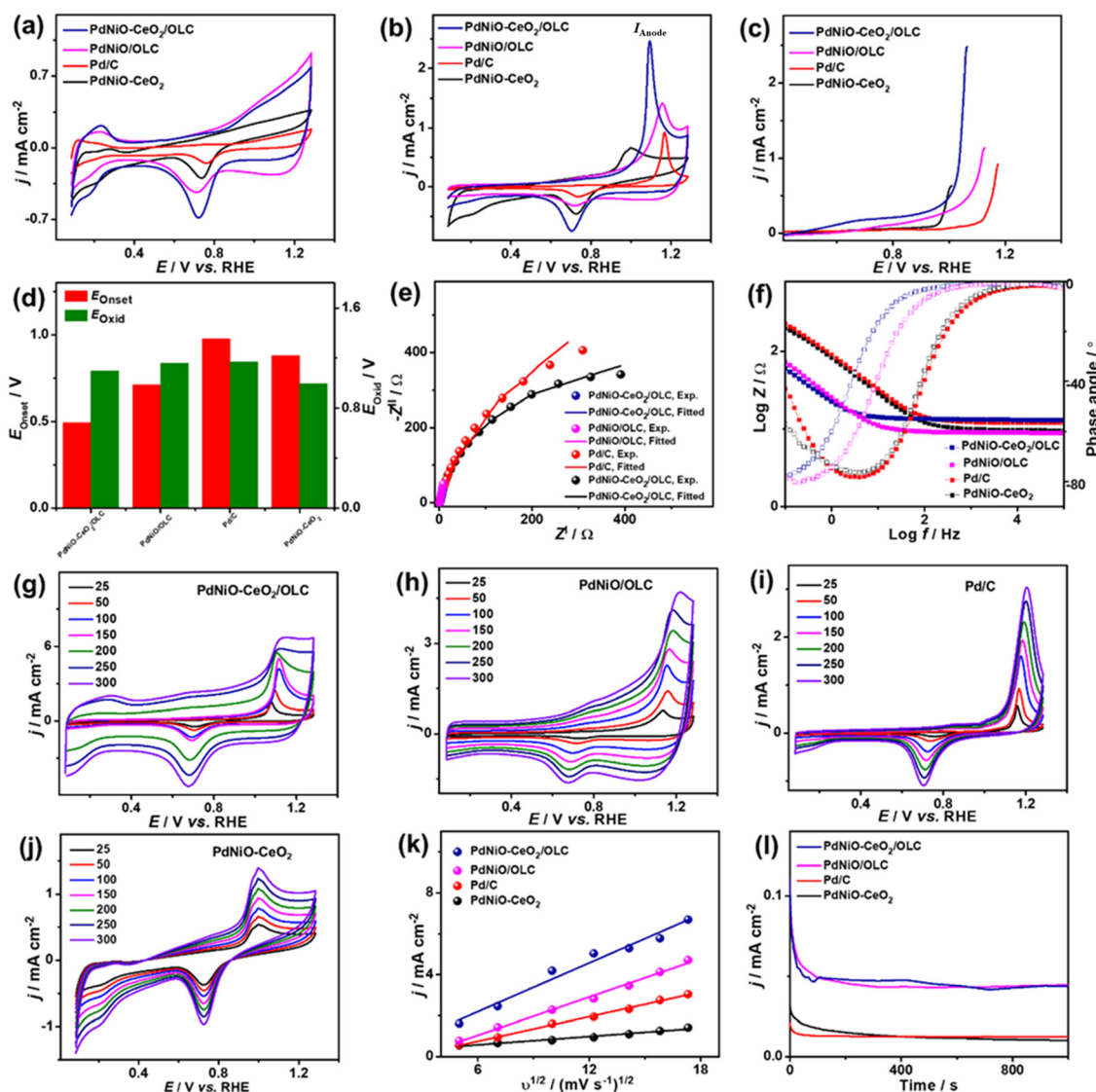

Fig. 3 CV profiles at 50 mV s^{-1} in (a) N$_2$-saturated HClO$_4$ (0.1 M) and (b) CO-saturated HClO$_4$ (0.1 M). (c) LSV at 50 mV s^{-1}. (d) E_{Onset} and E_{Oxid}. (e) Nyquist plots. (f) Bode plots. (g–j) Scan rate studies. (k) Randles–Sevcik plots (I_{Anode} vs. $\nu^{1/2}$). (l) CA of PdNiO–CeO$_2$/OLC, PdNiO/OLC, PdNiO–CeO, and PdC in CO-saturated HClO$_4$ (0.1 M).

3040 | Catal. Sci. Technol., 2023, **13**, 3035–3046

This journal is © The Royal Society of Chemistry 2023

ease of formation of Pd-oxygenated species, which is plausibly attributed to the O_2-rich CeO_2/OLC support that is highly desirable merit for enhanced CO_{oxid} performance.

The area of $H_{ads/des}$ for PdNiO–CeO_2/OLC is larger than those for PdNiO/OLC, PdNiO–CeO_2, and Pd/C, implying its higher surface area. The ECSA of PdNiO–CeO_2/OLC (12.64 m^2 g^{-1}) is higher than PdNiO/OLC (11.40 m^2 g^{-1}), PdNiO–CeO_2 (9.76 m^2 g^{-1}), and Pd/C (6.19 m^2 g^{-1}), implying its higher number of exposed active sites. The CV profiles of PdNiO–CeO_2/OLC, PdNiO/OLC, PdNiO–CeO_2, and Pd/C are evaluated in CO-saturated $HClO_4$ (0.1 M), which reveal intense anodic current densities (I_{Anode}) at higher potential assigned to oxidation of CO to CO_2 and weak peak in the reverse direction at lower potential (Fig. 3b). PdNiO–CeO_2/OLC has increased I_{Anode} (2.50 mA cm^{-2}), which is 1.74 times that of PdNiO/OLC (1.44 mA cm^{-2}), 3.73 times that of PdNiO–CeO_2 (0.67 mA cm^{-2}), and 2.63 times that of Pd/C (0.95 mA cm^{-2}), indicating the maximized utilization of active sites of PdNiO–CeO_2/OLC. This is evident in the LSV curves, which imply the ability of PdNiO–CeO_2/OLC to oxidize CO at a higher I_{Anode}, but a lower applied potential compared with PdNiO/OLC, PdNiO–CeO_2 and Pd/C (Fig. 3c). This implies the quick CO oxidation kinetics on PdNiO–CeO_2/OLC as further seen in its lower CO oxidation E_{Onset}/CO_{oxid} potential (E_{oxid}) (0.49 V/1.09 V) than PdNiO/OLC (0.71 V/1.16 V), PdNiO–CeO_2 (0.88 V/1.00 V), PdNiO–CeO_2 (0.80 V/0.99 V), and Pd/C (0.98 V/1.17 V) (Fig. 3d). This is owing to the synergism of PdNiO nanostructures, and their electronic interaction with CeO_2/OLC which facilitates the formation of oxygenated species and accelerates the charge mobility needed for promoting CO oxidation at low potential.

This is proved by the EIS studies conducted to get more insights into the interfacial interaction between the nanocatalysts during the electrooxidation of CO. The Nyquist plots of the obtained PdNiO–CeO_2/OLC, PdNiO/OLC, PdNiO–CeO_2, and Pd/C show deformed semi-circle curves in CO-saturated $HClO_4$ (0.1 M) (Fig. 3e). The EIS data are fitted by a Voigt electrical equivalent circuit (EEC) model to determine the solution resistance (R_s), charge transfer resistance (R_{ct}), and constant phase element (CPE) (Fig. S4a†). All the nanocatalysts have similar R_s values within the confinement of the error bars, implying the same ionic conductivity in the $HClO_4$ electrolyte. However, PdNiO–CeO_2/OLC has a lower R_{ct} (36.22 Ω) than PdNiO/OLC (52.90 Ω) and Pd/C (278.11 Ω), revealing lower charge transfer resistance and consequent better reaction kinetics on PdNi–CeO_2/OLC (Table 1).

Following the power law of CPE impedance: $Z_{CPE} = 1/(Q(j\omega)^n)$, with ideality factor n. The Pd-based nanocatalysts PdNiO–CeO_2/OLC (49.72 μS $s^{(1-a)}$) and PdNiO/OLC (43.05 μS $s^{(1-a)}$) possess high CPE impedance relative to PdNi–CeO_2 (18.44 μS $s^{(1-a)}$) and Pd/C (24.01 μS $s^{(1-a)}$), implying high charge transport on the roughness and porosity of multimetallic PdNi–CeO_2/OLC. This is evident in the Bode plots (Fig. 3f), which proved the lower overall impedance in the low-frequency region of PdNiO–CeO_2/OLC than PdNiO/OLC, and Pd/C. Also, the lower phase angle of PdNiO–CeO_2/OLC (75.9°) than that of PdNiO/OLC (80.8°), PdNiO–CeO_2 (82.7°), and Pd/C (83°) further proves superior diffusion of intermediates during CO oxidation on PdNiO–CeO_2/OLC. The diffusion of intermediate species on the nanocatalysts during CO electrooxidation is corroborated by measuring the CV curves at different scan rates (v, 25–300 mV s^{-1}), which disclose that I_{Anode} increases at high v (Fig. 3g–j). The Randles–Sevcik plots express the linear relationship between I_{Anode} and the square root of scan rate ($v^{1/2}$) that proves a diffusion-controlled process of CO on the tested nanocatalysts (Fig. 3k). Notably, PdNiO–CeO_2/OLC exhibits a higher slope (0.40) than PdNiO/OLC (0.31), PdNiO–CeO_2 (0.07), and Pd/C (0.20), evidencing the faster diffusion of CO intermediates on PdNiO–CeO_2/OLC.

The stability of CO electrooxidation on the catalysts was investigated by CA and accelerated stability test (AST) in CO-saturated $HClO_4$ (0.1 M) at 50 mV s^{-1}. The CA results show gradual CO oxidation activity loss on all the nanocatalysts at steady-state conditions, but with a lower degradation, besides preserving a higher current density, on PdNiO–CeO_2/OLC than PdNiO/OLC, PdNiO–CeO_2, and Pd/C (Fig. 3l). After 1000 stability cycles of CV curves in CO-saturated $HClO_4$ (0.1 M), PdNiO–CeO_2/OLC lost only 14.5% of its initial CO oxidation activity compared with PdNiO/OLC (27.8%), PdNiO–CeO_2 (25.0%), and Pd/C (37.9%) (Fig. S4b–f†). This indicates the superior CO oxidation durability of PdNiO–CeO_2/OLC as further proved by the TEM image obtained after AST, which showed the structural stability without any obvious morphological change (i.e., aggregation or attachment of PdNiO) (Fig. S4g†).

The CO_{oxid} electrocatalysis on the Pd-based nanocatalysts was investigated in KOH (0.1 M) medium. The CV curves measured in N_2-saturated KOH (0.1 M) of PdNiO–CeO_2/OLC, PdNiO/OLC, PdNiO–CeO_2, and Pd/C display the voltammogram of Pd with a noticeable negative shift of the Pd–O reduction peak of PdNiO–CeO_2/OLC relative to PdNiO/OLC, PdNiO–CeO_2, and Pd/C. This implies the ease of generating oxygenated species on Pd. The ECSA of PdNiO–

Table 1 EIS data for PdNiO–CeO_2/OLC, PdNiO/OLC, PdNiO–CeO_2, and Pd/C in CO-saturated $HClO_4$ (0.1 M)

	R_s (Ω)	R_{ct} (Ω)	CPE (μS $s^{(1-a)}$)	n
PdNiO–CeO_2/OLC	0.99 ± 0.07	36.22 ± 0.68	49.72 ± 2.31	0.80
PdNiO/OLC	1.02 ± 0.04	52.90 ± 0.52	43.05 ± 1.57	0.89
Pd/C	1.48 ± 0.75	278.11 ± 1.08	24.01 ± 0.22	0.90
PdNiO–CeO_2	1.28 ± 0.52	398.27 ± 3.32	18.44 ± 0.54	0.88

This journal is © The Royal Society of Chemistry 2023

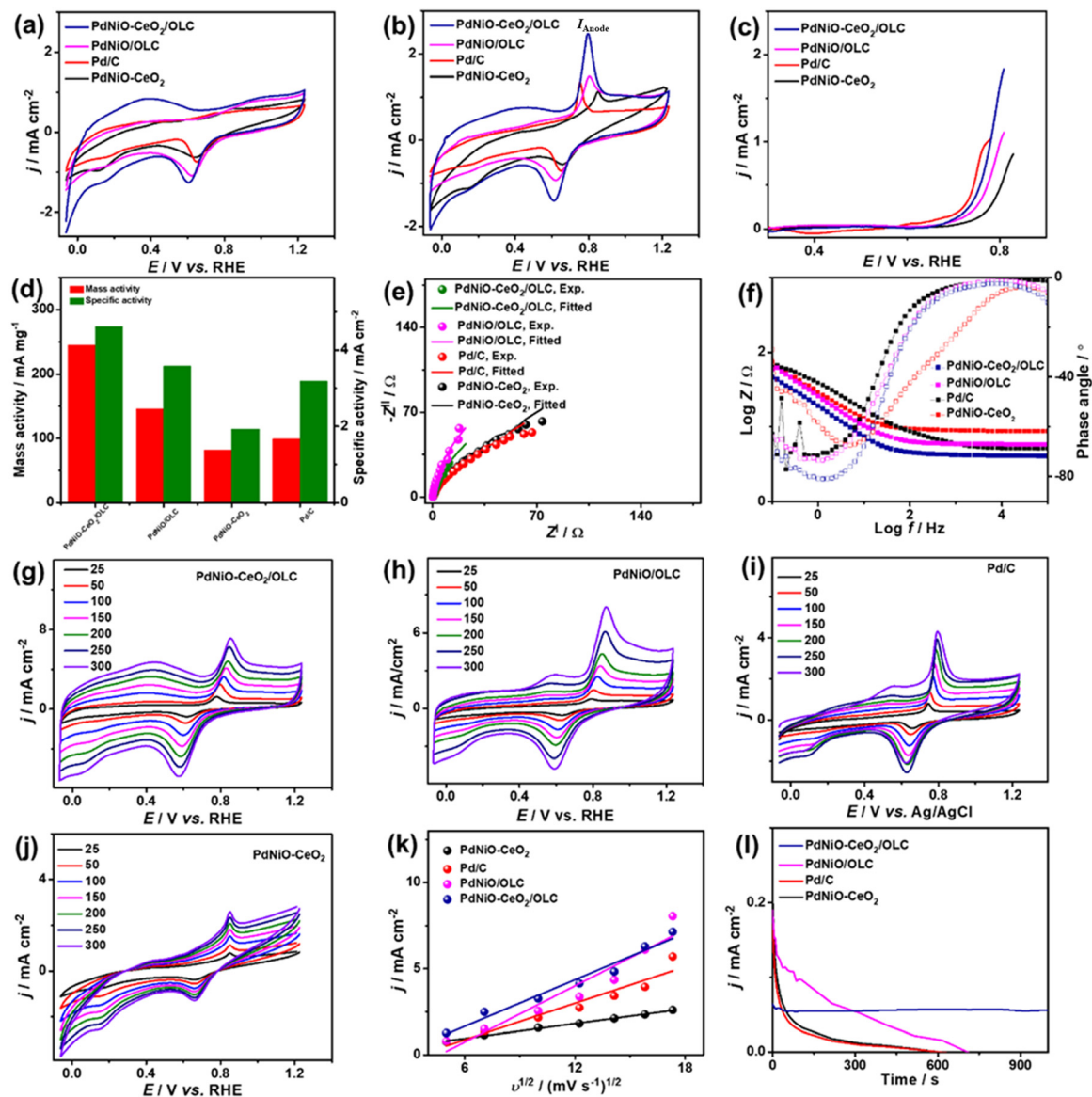*Catal. Sci. Technol.*, 2023, **13**, 3035–3046 | **3041**

Fig. 4 CV curves at 50 mV s^{-1} in (a) N$_2$-saturated KOH (0.1 M) and (b) CO-saturated KOH (0.1 M). (c) LSV at 50 mV s^{-1}. (d) Mass/specific activities. (e) Nyquist plots. (f) Bode plots. (g–j) Scan rate studies. (k) Randles–Sevcik plots (I_{Anode} vs. $v^{1/2}$) and (l) CA of PdNiO–CeO$_2$/OLC, PdNiO/OLC, PdNiO–CeO$_2$, and Pd/C in CO-saturated KOH (0.1 M).

CeO$_2$/OLC (53.09 m^2 g^{-1}) is greater than PdNiO/OLC (42.01 m^2 g^{-1}), PdNiO–CeO$_2$ (31.76 m^2 g^{-1}), and Pd/C (25.76 m^2 g^{-1}) (Fig. 4a). The CV profiles of the PdNiO–CeO$_2$/OLC, PdNiO/OLC, and Pd/C catalysts tested in CO-saturated KOH (0.1 M) show the CO oxidation features with a higher I_{Anode} (2.486 mA cm^{-2}) on PdNiO–CeO$_2$/OLC than on PdNiO/OLC (1.46 mA cm^{-2}), PdNiO–CeO$_2$ (1.12 mA cm^{-2}), and Pd/C (1.33 mA cm^{-2}) (Fig. 4b). Also, the LSV results display the lower E_{onset} on PdNiO–CeO$_2$/OLC (0.65 V) relative to PdNiO/OLC (0.68 V) and PdNiO–CeO$_2$ (0.71 V) along with a higher generated I_{Anode} than PdNiO–CeO$_2$ and Pd/C under any applied voltage point on PdNiO–CeO$_2$/OLC (Fig. 4c and d), indicating its faster CO electrooxidation kinetics. The mass (specific) activity of PdNiO–CeO$_2$/OLC (245 mA mg^{-1} (4.61 mA cm^{-2})) are higher than those of PdNiO/OLC (146 mA mg^{-1} (3.58 mA cm^{-2})),

PdNiO–CeO$_2$ (82 mA mg^{-1} (1.93 mA cm^{-2})), and Pd/C (99 mA mg^{-1} (3.19 mA cm^{-2})) (Fig. 4d). This is based on an equivalent Pd mass, which implies the maximized utilization of Pd in PdNiO–CeO$_2$/OLC, plausibly due to the porosity, electronic interaction, and higher concentration of surface sites.

The Nyquist plots show semi-circle curves but with a smaller diameter for PdNiO–CeO$_2$/OLC than PdNiO/OLC, PdNiO–CeO$_2$, and Pd/C in CO-saturated KOH (0.1 M), implying a better interfacial interaction between KOH electrolyte and PdNiO–CeO$_2$/OLC. The fitting of EIS data demonstrates the lower R_s/R_{ct} (0.98 Ω/45.52 Ω) for PdNiO–CeO$_2$/OLC than PdNiO/OLC, PdNiO–CeO$_2$, and Pd/C (Fig. 4e), indicating quicker CO$_{oxid}$ kinetics and faster charge mobility on PdNiO–CeO$_2$/OLC. This is validated by the Bode plots

3042 | *Catal. Sci. Technol.*, 2023, **13**, 3035–3046

This journal is © The Royal Society of Chemistry 2023

which depict the lower $\log Z$ in the low-frequency region for PdNiO–CeO$_2$/OLC than PdNiO/OLC, PdNiO–CeO$_2$, and Pd/C, in addition to a lower phase angle (67°), indicating the fast diffusion of reactants on PdNiO–CeO$_2$/OLC (Fig. 4f).

This is shown in the steady linear increase in I_{Anode} of the tested catalysts with increasing v from 25 to 300 mV s^{-1} and the linear relationship between I_{Anode} vs. $v^{1/2}$ (Fig. 4g–j). This demonstrates the diffusion-controlled process for CO electrooxidation on PdNiO–CeO$_2$/OLC, PdNiO/OLC, PdNiO–CeO$_2$, and Pd/C; however, the higher slope for PdNiO–CeO$_2$/OLC (0.45) implies its faster CO$_{oxid}$ kinetics (Fig. 4k). CA conducted in CO-saturated KOH (0.1 M) implies higher durability with lower degradation of I_{Anode} for PdNiO–CeO$_2$/OLC than PdNiO/OLC, PdNiO–CeO$_2$, and Pd/C (Fig. 4l).

Additionally, after 1000 CV cycles (AST), PdNiO–CeO$_2$/OLC retains 94.2% of its initial I_{Anode} compared to PdNiO/OLC (83.1%), PdNiO–CeO$_2$ (86.8%), and Pd/C (73.4%) (Fig. S5†).

The CV curves measured in N$_2$-saturated NaHCO$_3$ (0.1 M) on PdNiO–CeO$_2$/OLC, PdNiO/OLC, PdNiO–CeO$_2$, and Pd/C show the ideal voltammogram of Pd-based catalysts, but with an obvious higher peak area of PdO and negatively shifted peak on PdNiO–CeO$_2$/OLC than PdNiO/OLC, PdNiO–CeO$_2$, and Pd/C (Fig. 5a). This implies a higher surface area and ease of generation of oxygenated species on PdNiO–CeO$_2$/OLC and PdNiO/OLC. Thereby, the estimated ECSA are about 9.10, 6.78, 5.19, and 3.60 m^2 g^{-1} for PdNiO–CeO$_2$/OLC, PdNiO/OLC, PdNiO–CeO$_2$, and Pd/C, respectively. The CV curves measured in CO-saturated NaHCO$_3$ (0.1 M) disclose

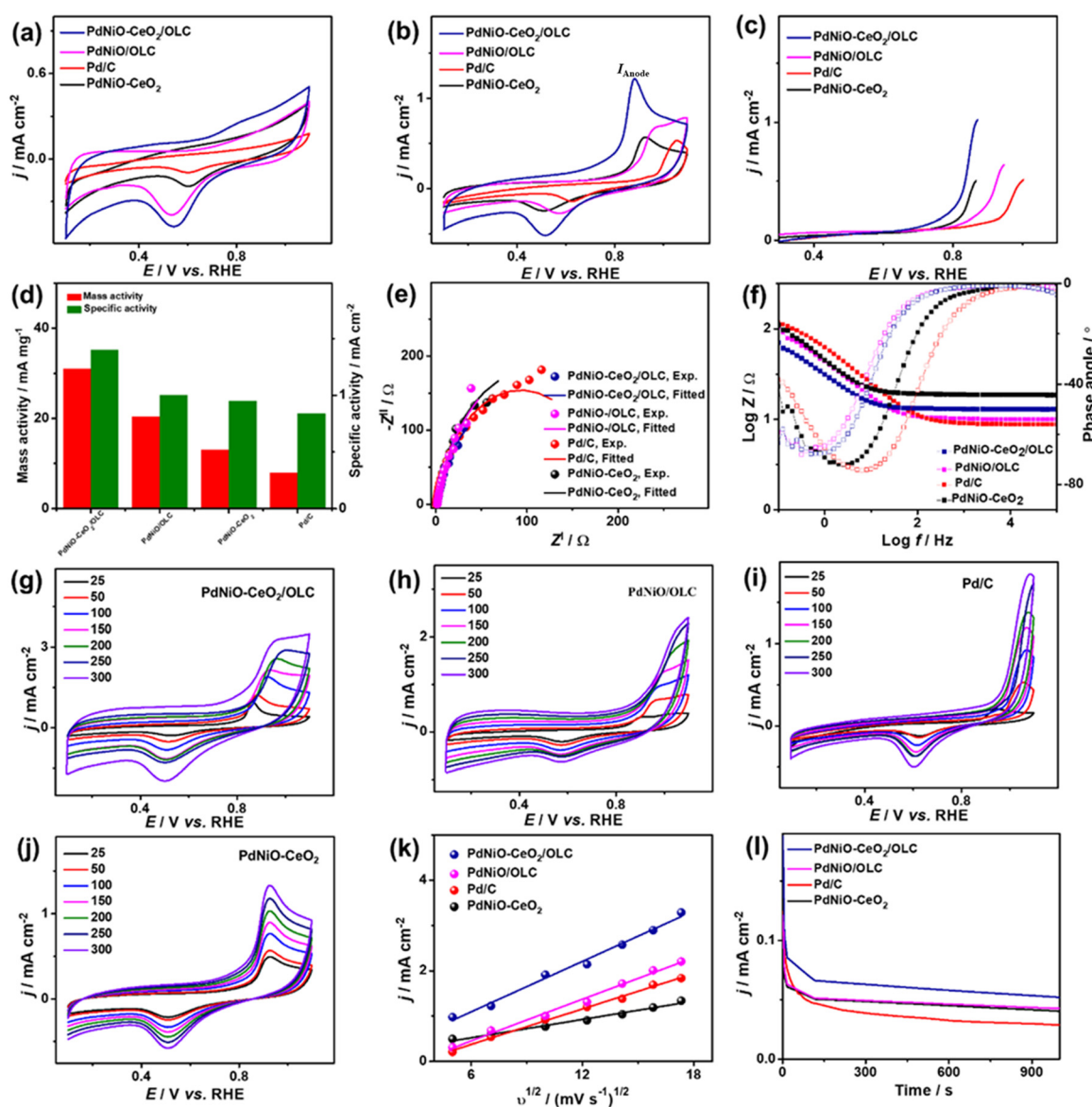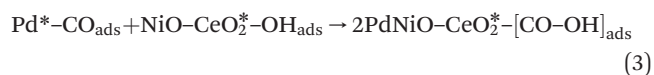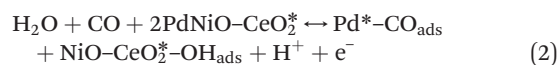

Fig. 5 CV profiles at 50 mV s^{-1} in (a) N$_2$-saturated NaHCO$_3$ (0.1 M) and (b) CO-saturated NaHCO$_3$ (0.1 M). (c) LSV at 50 mV s^{-1}. (d) Mass/specific activities. (e) Nyquist plots. (f) Bode plots. (g–j) Scan rate studies. (k) Randles–Sevcik plots (I_{Anode} vs. $v^{1/2}$) and (l) CA of PdNiO–CeO$_2$/OLC, PdNiO/OLC, PdNiO–CeO$_2$, and PdC in CO-saturated NaHCO$_3$ (0.1 M).

This journal is © The Royal Society of Chemistry 2023

Catal. Sci. Technol., 2023, 13, 3035–3046 | 3043

the CO oxidation voltammogram, but with a greater I_{Anode} on PdNiO–CeO$_2$/OLC (1.23 mA cm^{-2}) than PdNiO/OLC (0.69 mA cm^{-2}), PdNiO–CeO$_2$ (0.57 mA cm^{-2}), and Pd/C (0.54 mA cm^{-2}) by 1.76, 2.14, and 2.26 times correspondingly (Fig. 5b). The LSV test shows the ability of PdNiO–CeO$_2$/OLC to oxidize CO and generate higher I_{Anode} at a lower potential than PdNiO/OLC, PdNiO–CeO$_2$, and Pd/C (Fig. 5c), indicating faster CO electrooxidation kinetics on PdNiO–CeO$_2$/OLC.

The mass (specific) activity of PdNiO–CeO$_2$/OLC (31 mA mg^{-1} (1.40 mA cm^{-2})) are higher than those of PdNiO/OLC (20.34 mA mg^{-1} (1.00 mA cm^{-2})), PdNiO–CeO$_2$ (12.98 mA mg^{-1} (0.95 mA cm^{-2})), and Pd/C (7.92 mA mg^{-1} (0.84 mA cm^{-2})) (Fig. 5d). The Nyquist plots obtained in CO-saturated NaHCO$_3$ (0.1 M) show semi-circle curves, but with a lower diameter for PdNiO–CeO$_2$/OLC than PdNiO/OLC, PdNiO–CeO$_2$, and Pd/C, that could serve as evidence for the higher electrical conductivity. Fitting of EIS data using Voigt EEC displays the similar R_s of the tested catalysts but with smaller R_{ct} for PdNiO–CeO$_2$/OLC than PdNiO/OLC, PdNiO–CeO$_2$, and Pd/C, which indicates better electrolyte–electrode interaction and higher charge transfer on PdNiO–CeO$_2$/OLC (Fig. 5e and Table S2†). This is also seen in the higher CPE impedance of PdNiO–CeO$_2$/OLC (47.76 μS s$^{(1-a)}$) than those of PdNiO/OLC (40.71 μS s$^{(1-a)}$), PdNiO–CeO$_2$ (25.78 μS s$^{(1-a)}$), and Pd/C (37.74 μS s$^{(1-a)}$) as further confirmed in the Bode plots, where PdNiO–CeO$_2$/OLC exhibits low $\log Z$ in the low-frequency range alongside a lower phase angle (65.2°) relative to PdNiO/OLC (67.4°), PdNiO–CeO$_2$ (71.8°), and Pd/C (74.7°) (Fig. 5f). This implies a better diffusion of reactants on the porous PdNiO–CeO$_2$/OLC during CO$_{oxid}$.

The increase in I_{Anode} with increasing v from 25 to 250 mV s^{-1} on PdNiO–CeO$_2$/OLC, PdNiO/OLC, PdNiO–CeO$_2$, and Pd/C along with the linear relationship of I_{Anode} vs. $v^{1/2}$ reveal a diffusion-controlled mechanism for the electrooxidation of CO (Fig. 5g–j). However, a greater slope for PdNiO–CeO$_2$/OLC (0.19) than PdNiO/OLC (0.15), PdNiO–CeO$_2$ (0.09), and Pd/C (0.13) (Fig. 5k) implies the improved diffusion of reactants and intermediate species on PdNiO–CeO$_2$/OLC during CO$_{oxid}$. CA measured in CO-saturated NaHCO$_3$ (0.1 M) for 1000 s displays the lower degradation of I_{Anode} on PdNiO–CeO$_2$/OLC than PdNiO/OLC, PdNiO–CeO$_2$, and Pd/C (Fig. 5l). Meanwhile, after 1000 CO oxidation durability cycles, PdNiO–CeO$_2$/OLC only lost 15.6% of its initial catalytic activity compared with PdNiO/OLC (27.6%), PdNiO–CeO$_2$ (18.0%), and Pd/C (32.2%) (Fig. S6†). PdNiO–CeO$_2$/OLC retained 84% of its initial ECSA relative to PdNiO/OLC (72%), PdNiO–CeO$_2$ (82%), and Pd/C (68%) in addition to the absence of any voltammogram features related to degradation of PdNiO.

The CO electrooxidation results for PdNiO–CeO$_2$/OLC, PdNiO/OLC, and PdNiO–CeO$_2$ are compared with previous findings in the literature (Table S3†). The CO oxidation on PdNiO–CeO$_2$/OLC is proposed to follow the Langmuir–Hinshelwood mechanism, presented in eqn (2)–(4):[59]

$$H_2O + CO + 2PdNiO-CeO_2^* \leftrightarrow Pd^*-CO_{ads} + NiO-CeO_2^*-OH_{ads} + H^+ + e^- \quad (2)$$

$$Pd^*-CO_{ads} + NiO-CeO_2^*-OH_{ads} \rightarrow 2PdNiO-CeO_2^*-[CO-OH]_{ads} \quad (3)$$

$$PdNiO-CeO_2^*-[CO-OH]_{ads} \leftrightarrow CO_2 + H^+ + PdNiO-CeO_2^* + e^- \quad (4)$$

where "*" and "$_{ads}$" represent the nanocatalyst's active sites and adsorbed species, respectively.

Conclusion

This article presents the controlled synthesis of ternary PdNiO nanocrystals supported on porous CeO$_2$/onion-like carbon (PdNiO–CeO$_2$/OLC) nanostructures based on the sol–gel, annealing, and impregnation approaches. Under typical conditions, flower-like CeO$_2$/OLC supported the growth of PdNiO nanocrystals without the need for reducing agents or surfactants. This leads to the formation of porous sponge-like PdNiO–CeO$_2$/OLC, coupled with the unique merits of multifunctional structures, low mass of Pd (10 wt%), pore volume (0.30 m^3 g^{-1}), and great BET surface area (155.66 m^2 g^{-1}). The effects of supports and electrolytes on the CO$_{oxid}$ activity and durability of PdNiO–CeO$_2$/OLC were investigated. The electrocatalytic CO$_{oxid}$ activity of PdNiO–CeO$_2$/OLC was superior to those of PdNiO/OLC by at least 1.66 times, PdNiO–CeO$_2$ by at least 1.88 times, and commercial Pd/C by at least 2.12 times in all electrolytes, besides great durability after 1000 cycles. This is owing to the electronic interaction of PdNiO with the CeO$_2$/OLC support, which eases CO adsorption/activation, alongside activation/dissociation of H$_2$O to generate active oxygenated species (i.e., OH) needed for accelerating CO$_{oxid}$ kinetics. Also, the CO$_{oxid}$ of PdNiO–CeO$_2$/OLC in different electrolytes followed the order of HClO$_4$ > KOH > NaHCO$_3$. This study may allow the synthesis of other ternary Pd-based electrocatalysts for CO oxidation along with an understanding of the effect of supports and electrolytes.

Conflicts of interest

We declare no conflicts of interest.

Acknowledgements

References

1 K. Eid, Y. H. Ahmad, S. Y. AlQaradawi and N. K. Allam, *Catal. Sci. Technol.*, 2017, 7, 2819–2827.

3044 | *Catal. Sci. Technol.*, 2023, **13**, 3035–3046

This journal is © The Royal Society of Chemistry 2023

2 K. Eid, K. A. Soliman, D. Abdulmalik, D. Mitoraj, M. H. Sleim, M. O. Liedke, H. A. El-Sayed, A. S. AlJaber, I. Y. Al-Qaradawi and O. M. Reyes, *Catal. Sci. Technol.*, 2020, **10**, 801–809.

3 M. A. Ahsan, T. He, K. Eid, A. M. Abdullah, M. F. Sanad, A. Aldalbahi, B. Alvarado-Tenorio, A. Du, A. R. Puente Santiago and J. C. Noveron, *ACS Appl. Mater. Interfaces*, 2022, **14**, 3919–3929.

4 F. Wu, K. Eid, A. M. Abdullah, W. Niu, C. Wang, Y. Lan, A. A. Elzatahry and G. Xu, *ACS Appl. Mater. Interfaces*, 2020, **12**, 31309–31318.

5 Q. Lu, J. Li, K. Eid, X. Gu, Z. Wan, W. Li, R. S. Al-Hajri and A. M. Abdullah, *J. Electroanal. Chem.*, 2022, **916**, 116361.

6 S. Sharma, M. Groves, J. Fennell, N. Soin, S. Horswell and C. Malardier-Jugroot, *Chem. Mater.*, 2014, **26**, 6142–6151.

7 A. K. Ipadeola, R. Barik, S. C. Ray and K. I. Ozoemena, *Electrocatalysis*, 2019, **10**, 366–380.

8 K. I. Ozoemena, S. Musa, R. Modise, A. K. Ipadeola, L. Gaolatlhe, S. Peteni and G. Kabongo, *Curr. Opin. Electrochem.*, 2018, **10**, 82–87.

9 K. Eid, Y. H. Ahmad, H. Yu, Y. Li, X. Li, S. Y. AlQaradawi, H. Wang and L. Wang, *Nanoscale*, 2017, **9**, 18881–18889.

10 H. J. Freund, G. Meijer, M. Scheffler, R. Schlögl and M. Wolf, *Angew. Chem., Int. Ed.*, 2011, **50**, 10064–10094.

11 R. M. Al Soubaihi, K. M. Saoud, M. T. Z. Myint, M. A. Göthelid and J. Dutta, *Catalysts*, 2021, **11**, 131.

12 J. Lin, B. Qiao, L. Li, H. Guan, C. Ruan, A. Wang, W. Zhang, X. Wang and T. Zhang, *J. Catal.*, 2014, **319**, 142–149.

13 A. K. Ipadeola, M. Chitt, A. Abdelgawad, K. Eid and A. M. Abdullah, *Int. J. Hydrogen Energy*, 2023, DOI: **10.1016/j.ijhydene.2023.01.208**, (in press).

14 K. Eid, A. Gamal and A. M. Abdullah, *Green Chem.*, 2023, **25**, 1276–1310.

15 Y. Zhang, Y. Cai, Y. Guo, H. Wang, L. Wang, Y. Lou, Y. Guo, G. Lu and Y. Wang, *Catal. Sci. Technol.*, 2014, **4**, 3973–3980.

16 C. Hudy, J. Gryboś, K. Steenbakkers, K. Góra-Marek, F. Zasada and Z. Sojka, *Catal. Sci. Technol.*, 2022, **12**, 5723–5741.

17 B. Singh, V. Sharma, R. P. Gaikwad, P. Fornasiero, R. Zboril and M. B. Gawande, *Small*, 2021, **17**, 2006473.

18 R. G. dos Santos and A. C. Alencar, *Int. J. Hydrogen Energy*, 2020, **45**, 18114–18132.

19 Q. Lu, K. Eid, W. Li, A. M. Abdullah, G. Xu and R. S. Varma, *Green Chem.*, 2021, **23**, 5394–5428.

20 K. Eid, M. H. Sliem, M. Al-Ejji, A. M. Abdullah, M. Harfouche and R. S. Varma, *ACS Appl. Mater. Interfaces*, 2022, **14**, 40749–40760.

21 K. Eid, M. H. Sliem and A. M. Abdullah, *Nanoscale*, 2019, **11**, 11755–11764.

22 A. K. Ipadeola, K. Eid, A. M. Abdullah and K. I. Ozoemena, *Langmuir*, 2022, **38**, 11109–11120.

23 P. Van der Wal, N. De Rooij and M. Koudelka-Hep, *Sens. Actuators, B*, 1996, **35**, 119–123.

24 A. Abdelgawad, B. Salah, K. Eid, A. M. Abdullah, R. S. Al-Hajri, M. Al-Abri, M. K. Hassan, L. A. Al-Sulaiti, D. Ahmadaliev and K. I. Ozoemena, *Int. J. Mol. Sci.*, 2022, **23**, 15034.

25 A. K. Ipadeola, P. V. Mwonga and K. I. Ozoemena, *Electrochim. Acta*, 2021, **390**, 138860.

26 E. Madrid, C. Harabajiu, R. S. Hill, K. Black, L. Torrente-Murciano, A. J. Dickinson, P. J. Fletcher, K. I. Ozoemena, A. K. Ipadeola and E. Oguzie, *ChemElectroChem*, 2021, **8**, 378–385.

27 A. K. Ipadeola, P. V. Mwonga, S. C. Ray, R. R. Maphanga and K. I. Ozoemena, *Electroanalysis*, 2020, **32**, 3060–3074.

28 Y. Zhou, Z. Wang and C. Liu, *Catal. Sci. Technol.*, 2015, **5**, 69–81.

29 B. Salah, K. Eid, A. M. Abdelgwad, Y. Ibrahim, A. M. Abdullah, M. K. Hassan and K. I. Ozoemena, *Electroanalysis*, 2022, **34**, 677–683.

30 Y.-J. Wang, N. Zhao, B. Fang, H. Li, X. T. Bi and H. Wang, *Chem. Rev.*, 2015, **115**, 3433–3467.

31 M. G. Hosseini, F. Hosseinzadeh, P. Zardari and M. Darbandi, *Int. J. Hydrogen Energy*, 2021, **46**, 28513–28526.

32 C. Han, J. Zenner, J. Johny, N. Kaeffer, A. Bordet and W. Leitner, *Nat. Catal.*, 2022, **5**, 1110–1119.

33 J. K. McDonough and Y. Gogotsi, *Electrochem. Soc. Interface*, 2013, **22**, 61.

34 N. Keller, N. I. Maksimova, V. V. Roddatis, M. Schur, G. Mestl, Y. V. Butenko, V. L. Kuznetsov and R. Schlögl, *Angew. Chem., Int. Ed.*, 2002, **41**, 1885–1888.

35 I. Choi, *Int. J. Hydrogen Energy*, 2019, **44**, 26589–26596.

36 J. M. Jaksic, N. V. Krstajic, L. M. Vracar, S. G. Neophytides, D. Labou, P. Falaras and M. M. Jaksic, *Electrochim. Acta*, 2007, **53**, 349–361.

37 Y. Jin, G. Sun, F. Xiong, L. Ding and W. Huang, *Eur. J. Chem.*, 2015, **21**, 4252–4256.

38 K. Polychronopoulou, C. N. Costa and A. M. Efstathiou, *Catal. Today*, 2006, **112**, 89–93.

39 S. Zeng, Y. Wang, S. Ding, J. J. Sattler, E. Borodina, L. Zhang, B. M. Weckhuysen and H. Su, *J. Power Sources*, 2014, **256**, 301–311.

40 C.-J. Jia, M. Schwickardi, C. Weidenthaler, W. Schmidt, S. Korhonen, B. M. Weckhuysen and F. Schüth, *J. Am. Chem. Soc.*, 2011, **133**, 11279–11288.

41 D. Gu, J.-C. Tseng, C. Weidenthaler, H.-J. Bongard, B. Spliethoff, W. Schmidt, F. Soulimani, B. M. Weckhuysen and F. Schüth, *J. Am. Chem. Soc.*, 2016, **138**, 9572–9580.

42 A. K. Ipadeola, K. Eid, A. K. Lebechi, A. M. Abdullah and K. I. Ozoemena, *Electrochem. Commun.*, 2022, **140**, 107330.

43 A. K. Ipadeola, A. K. Lebechi, L. Gaolatlhe, A. B. Haruna, M. Chitt, K. Eid, A. M. Abdullah and K. I. Ozoemena, *Electrochem. Commun.*, 2022, **136**, 107207.

44 K. Eid, H. Wang, V. Malgras, Z. A. Alothman, Y. Yamauchi and L. Wang, *J. Phys. Chem. C*, 2015, **119**, 19947–19953.

45 A. K. Lebechi, A. K. Ipadeola, K. Eid, A. M. Abdullah and K. I. Ozoemena, *Nanoscale*, 2022, **14**, 10717–10737.

46 A. K. Ipadeola, P. V. Mwonga, S. C. Ray, R. R. Maphanga and K. I. Ozoemena, *ChemElectroChem*, 2020, **7**, 4562–4571.

47 J. J. Ogada, A. K. Ipadeola, P. V. Mwonga, A. B. Haruna, F. Nichols, S. Chen, H. A. Miller, M. V. Pagliaro, F. Vizza, J. R.

This journal is © The Royal Society of Chemistry 2023

Catal. Sci. Technol., 2023, **13**, 3035–3046 | **3045**

Varcoe, D. M. Meira, D. M. Wamwangi and K. I. Ozoemena, *ACS Catal.*, 2022, **12**, 7014–7029.

48 J. M. Jaksic, D. Labou, G. D. Papakonstantinou, A. Siokou and M. M. Jaksic, *J. Phys. Chem. C*, 2010, **114**, 18298–18312.

49 H. Na, H. Choi, J.-W. Oh, Y. S. Jung and Y. S. Cho, *ACS Appl. Mater. Interfaces*, 2019, **11**, 25179–25185.

50 Y. Martynova, S. Shaikhutdinov and H. J. Freund, *ChemCatChem*, 2013, **5**, 2162–2166.

51 L. P. Herrera, L. F. d. L. e Freitas, J. Hong, A. S. Hoffman, S. R. Bare, E. Nikolla and J. W. Medlin, *Catal. Sci. Technol.*, 2022, **12**, 1476–1486.

52 C. Xu, Z. Tian and P. Shen, *Electrochim. Acta*, 2008, **53**, 2610–2618.

53 W. Zou, C. Ge, M. Lu, S. Wu, Y. Wang, J. Sun, Y. Pu, C. Tang, F. Gao and L. Dong, *RSC Adv.*, 2015, **5**, 98335–98343.

54 F. Yang, X. Zhang, L. Zhou, S. Lin, X. Cao, J. Jiang and X. Lu, *Chem. Eng. J.*, 2022, **432**, 134255.

55 A. S. Ismail, I. Garcia-Torregrosa, J. C. Vollenbroek, L. Folkertsma, J. G. Bomer, T. Haarman, M. Ghiasi, M. Schellhorn, M. Nachtegaal and M. Odijk, *ACS Catal.*, 2021, **11**, 12324–12335.

56 A. K. Ipadeola, K. Eid, A. M. Abdullah, R. S. Al-Hajri and K. I. Ozoemena, *Nanoscale Adv.*, 2022, **4**, 5044–5055.

57 M. Lepage, T. Visser, F. Soulimani, A. M. Beale, A. Iglesias-Juez, A. M. van der Eerden and B. M. Weckhuysen, *J. Phys. Chem. C*, 2008, **112**, 9394–9404.

58 M. Hantel, V. Presser, J. McDonough, G. Feng, P. T. Cummings, Y. Gogotsi and R. Kötz, *J. Electrochem. Soc.*, 2012, **159**, A1897.

59 B. N. Grgur, N. M. Marković, C. A. Lucas and P. N. Ross Jr, *J. Serb. Chem. Soc.*, 2001, **66**, 785–797.